Heteroleptic NIR-Emitting Yb III /Anilate-Based Neutral Coordination Polymer Nanosheets for Solvent Sensing

Suchithra Ashoka Sahadevan, Noemi Monni, Mariangela Oggianu, Alexandre Abhervé, Daniela Marongiu, Michele Saba, Andrea Mura, Giovanni Bongiovanni, Valentina Mameli, Carla Cannas, et al.

Heteroleptic NIR-Emitting Yb^{III}/Anilate-based Neutral Coordination Polymer Nanosheets for Solvent Sensing

Suchithra Ashoka Sahadevan,[†] Noemi Monni,[†] Mariangela Oggianu,[†] Alexandre Abhervé,[‡] Daniela Marongiu, [‖]Michele Saba, [‖] Andrea Mura, [‖] Giovanni Bongiovanni,[‖] Valentina Mameli,[†] Carla Cannas,[†#] NarcisAvarvari,[‡] Francesco Quochi*[‖] and Maria Laura Mercuri*[†]*

[†]Dipartimento di Scienze Chimiche e Geologiche, Università degli Studi di Cagliari, S.S. 554 − Bivio per Sestu −I09042 Monserrato (Cagliari), Italy

[‡]Laboratoire MOLTECH-Anjou UMR 6200, UFR Sciences, CNRS, Université d'Angers, Bât. K, 2 Bd. Lavoisier, 49045 Angers,France

[‖]*Dipartimento di Fisica, Università degli Studi di Cagliari, I -09042 Monserrato (Cagliari), Italy*

[#]INSTM, Cagliari Unit, Via Giuseppe Giusti, 9, 50121 Firenze, Italy.

KEYWORDS: Coordination polymers, anilates, NIR-emitting lanthanides, carboxylates, nanosheets, photophysics

ABSTRACT. Nanosheets of two ~~novel~~ mixed linker (anilate/carboxylate)/Yb^{III}-based 2D layered coordination polymers (CPs) are herein reported. Bulky sized CPs, formulated as $[Yb_4(ClCNAn)_5(DOBDC)_1(DMSO)_{10}]_n \cdot (DMSO)_2$ (**1**) and $[Yb_2(ClCNAn)_2(F_4\text{-}BDC)(DMSO)_6]_n$(**2**), ~~consist of~~ are formed by two dimensional neutral polymeric ~~2D~~ networks ~~of~~ based on Yb^{III} ions, ~~alternating with both~~ heterosubstituted $ClCNAn^{2-}$ anilate and dicarboxylate linkers ($DOBDC^{2-}$ in **1**; F_4BDC^{2-} in **2**): in **1** neighbor layers are eclipsed and form six-membered rings showing either hexagonal cavities, formed by $ClCNAn^{2-}$ and Yb^{III} ions or rectangular cavities formed by $ClCNAn^{2-}$, $DOBDC^{2-}$ and Yb^{III} while distorted square-like cavities formed by $ClCNAn^{2-}$, F_4BDC^{2-} and Yb^{III} are ~~formed~~ obtained in **2**. **1-2** nanosheets, ~~hereafter~~ *i.e.* **1-NS** and **2-NS**, are ~~fabricated~~ produced by exfoliation of bulk CPs by the well-known top-down approach and characterized by AFM and HR-TEM. **1-2-NS** show thickness in the range of 1-5 nm, while the lateral dimensions are in the micrometer scale ~~thicknesses down to the monolayer~~ and the presence of well-defined lattice fringes, a key evidence of their robustness. Remarkably the PXRD patterns highlight that the crystallinity is retained at the nanoscale level. Nanosheets photophysics is investigated by an innovative Multiprobe Approach where lifetime, photoluminescence (PL) and integrate PL are simultaneously measured in order to study how these parameters can be affected by the presence of the different ligands. These advanced photophysical studies pave the way to challenging luminescent sensing applications and contribute to the ongoing research on fabricating robust and crystalline hybrid (organic/inorganic) lanthanide sheet-like 2D nanomaterials.

Introduction

Coordination Polymers (CPs) and Metal-Organic Frameworks(MOFs) have been an attractive field of current investigation due to their promising applications[1,2] ~~in several fields ranging from~~ in gas adsorption,[1] separation[3] and storage[4], ~~to~~ catalysis[5] and biomedicine.[6] Their crystalline frameworks, holding intriguing structures, depend mainly on the linkers/ligands and/or the metal ions. In particular, dicarboxylates, such as terephthalic acid (benzene-1,4-dicarboxylic acid=H_2BDC) and its derivative, 2,5-dihydroxy terephthalic acid (2,5-dihydroxy benzene-1,4-dicarboxylic acid=H_4DOBDC), have been successfully used to build ~~for the synthesis of~~ stable three-dimensional (3D) MOFs such as MOF-5,[7] MIL-53,[8,9] MIL-100.,[10,11] Furthermore M_2(*m*-DOBDC) and M_2(DOBDC) (M^{II} = Mn, Fe, Co, Ni) ~~), showing~~ have been shown to be highly porous MOFs, with BET surface area ~~ranging from~~ in the 1102 m^2/g (Mn_2(DOBDC) - 1349 m^2/g (Mn_2(*m*-DOBDC)[12] range and, noteworthy, ~~for constructing~~ luminescent MOFs[13,14] with lanthanide ions such as [Ln_2(DOBDC)$_3$(DMF)$_4$]DMF[15] (Ln = La,Ce, Pr, Nd, Gd) have been reported. Lanthanide MOFs/CPs,[14,16] ~~hereafter~~ *i.e.* Ln-MOFs, are of great interest for their applications as OLEDs,[17] sensors[18] and in biomedical analyses and cell imaging.[19,20] A strategy for the sensitization of Ln-MOFs is to incorporate π-conjugated organic molecules as suitable linkers, acting as antennas. With this view, fluorinated linkers ~~have attracted increasing attention~~ have been widely investigated, ~~as~~ since these compounds are supposed to show enhanced adsorption and luminescence properties[21–25] ~~as well as improved luminescence[25]~~ ~~compared to~~ than CPs with classical linkers, due to the fact that C–H vibrational quenchers are not present. [26] ~~quenching, which is typically an IR quencher, is not present.~~ 2,3,5,6 tetrafluoroterephthalic acid (2,3,5,6-tetrafluorobenzene-1,4-dicarboxylic acid= H_2F_4BDC), is, therefore, a very challenging ligand, scarcely investigated as MOF linker. ~~and~~ Only few series of Ln-CPs/MOFs are reported, ~~to the best of our knowledge,~~ such as [Ln(F_4BDC)$_{1.5}$(H_2O)$_n$]·mH_2O}n (Ln= Ce –Yb, n=2, m=1;

Ln = Pr and Nd, n= 1, m=2),[26] $[Ln(F_4BDC)(NO_3)(sol)_2]\cdot G$ (Ln^{III} = Eu, Gd, Tb, Ho, Tm, sol = DMF; Ln^{III}= Ho, Er and Tm, sol = DMSO) and $[Ln(F_4BDC)(CH_3COO)(FA)_3]\cdot 3FA$, ($Ln^{III}$ = Sm, Eu, FA = formamide).[27]

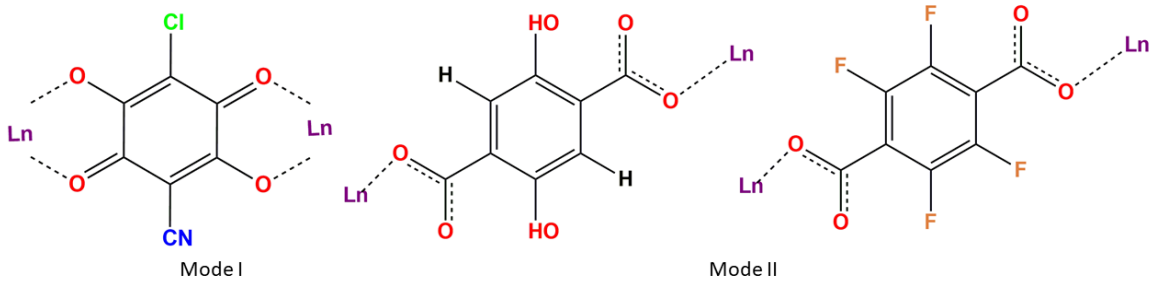

Chart 1. Coordination modes of $ClCNAn^{2-}$, $DOBDC^{2-}$, F_4-BDC^{2-} observed for **1** and **2**

Very recently we have reported on the ability of 3,6-disubstituted-2,5-dihydroxy-1,4-benzoquinone derivatives,[28–34] ~~hereafter called~~ also known as anilates, to construct 2D layered architectures[35–39] with lanthanides[40–46]. ~~and~~ The light-harvesting capability of the heterosubstituted 3-chloro-6-cyano-2,5-dihydroxybenzoquinone $ClCNAn^{2-}$,[31] ~~the first heterosubstituted ligand in the anilate family~~, towards NIR emissive Er^{III}, Yb^{III} and Nd^{III} ions,[47] was highlighted yielding 2D $[Ln_2(ClCNAn)_3(DMF)_6]\cdot(DCM)_x\}_n$ (Ln^{III} = Yb(x = 0), Nd, and Er (x = 2)) CPs. Interestingly these 2D CPs have been delaminated to produce ultrathin nanosheets with lateral sizes and thicknesses in the micrometer and nanometer range, respectively ~~of the micrometer scale and up to the monolayer~~ and bulk/nanosheets photophysical properties have been investigated. Nanosheet technology is a challenging task, despite the ongoing research on bulk MOFs/CPs, for luminescent sensing applications. ~~since they~~ Nanosheets show high surface/thickness ratio ~~leading to~~ ~~with larger surface areas~~ than the corresponding bulk-MOFs/CPs with several ~~and more accessible~~ active sites available to interact with target analytes (including metal ions, organic solvents, etc.) and therefore to ~~realize~~ provide fast-response

luminescent sensors with high sensitivity ~~highly sensitive and fast-response luminescent sensors, mainly when compared with~~. Furthermore, suspensions of these MOFs/CPs can be easily obtained in water or other organic solvents, with the possibility of their deposition on solid substrates for developping ultrathin nano-devices. ~~nanosheets can be easily dispersive in water or other organic solvents and can be easily deposited to fabricate ultrathin nano-devices. even though~~ Note that robust and crystalline sheets-like 2D nanomaterials[48] are required in order to be successfully used as reliable nanoplatforms for biomedical (drug delivery)[49–51]and sensing applications [52,53].

Nanosheets of two novel mixed linker (anilate/carboxylate) –Yb^{III}-based 2D neutral layered CPs, formulated as $[Yb_4(ClCNAn)_5(DOBDC)_1(DMSO)_{10}]_n.(DMSO)_2$ (**1**) and $[Yb_2(ClCNAn)_2(F_4\text{-}BDC)(DMSO)_6]_n$(**2**), hereafter **1-NS** and **2-NS**, are reported. The synthesis, structural characterization and photophysical studies of the corresponding bulky sized **1** and **2**, obtained *via* conventional one-pot synthetic methods, by reacting Yb^{III} ion with $ClCNAn^{2-}$, $DOBDC^{2-}$ or $F4BDC^{2-}$ organic linkers, shown in **Chart 1**, are also reported. The choice of the anilate/carboxylate mixed linkers ~~()~~ is crucial for determining either the dimensionality (2D) of the obtained CPs or to produce crystalline and robust nanosheets, a fundamental prerequisite for technological applications~~.~~ These peculiar features are accomplished taking advantage of the well-known ability of ~~*i) the*~~ anilate to form 2D networks and ~~the *ii) the*~~ carboxylate to form stable MOFs (the MILs family, *vide supra*), ~~respectively~~. Exfoliation of the fully characterized **1-2**bulk CPs was achieved by adopting a top-down strategy, the well-known sonication-assisted solution method. ~~is performed by using the well-known top-down strategy involving the traditional sonication-assisted solution method. and **1-2-NS are characterized** by~~ Atomic force microscopy (AFM), powder X-ray diffraction (PXRD) and high-resolution transmission electron

microscopy (HR-TEM) have been used to characterize **1-2 NS**. The intrinsic photophysical properties of bulk CPs are conventionally investigated. ~~while~~ Deep insight onto ~~the~~ **1-2-NS** photophysics, ~~of~~ as isopropanol suspensions, is gained by an innovative multiprobe approach by adding different solvents, either aliphatic or aromatic, allowing to shed light onto the role played by the different linkers in the Ln^{III} emission sensitization process. ~~This~~ The present work contributes to the ongoing research on hybrid (organic/inorganic) ultrathin nanosheets and provides guidelines for fabricating robust and crystalline sheet-like nanoplatforms as valuable prototypes for combining nanosheet technology with NIR-emitters-based luminescent sensing applications.

Results and Discussions

Synthesis.

Compound **1** was obtained in two steps. First, the one-pot reaction of H_4DOBDC, KHClCNAn, NaOH and Yb^{III} salts in water afforded a reddish crystalline powder. Small crystals could be analyzed by single-crystal XRD, yet the structure was of poor quality. It revealed, however, that the compound was a dinuclear cationic Yb^{III} complex, with one bridging $ClCNAn^{2-}$ ligand, two terminal H_3DOBDC^- ligands, ten coordinated water molecules and two chlorine counter-anions (structure not reported). In a second step, this crystalline sample was recrystallized in DMSO to get red crystals of CP **1 (Scheme 1)**. Compound **2** was obtained in a same way by using H_2F_4BDC instead of H_4DOBDC. The synthetic procedures are reported in the Experimental Section in SI. The $[Yb_4(ClCNAn)_5(DOBDC)_1(DMSO)_{10}]_n.(DMSO)_2$ (**1**) and $[Yb_2(ClCNAn)_2(F_4\text{-}BDC)(DMSO)_6]_n$ compounds (**2**) are neutral polymeric 2D porous networks.

~~Compound **1** was obtained by one-pot reaction of H_4DOBDC, KHClCNAn, NaOH and Yb^{III} salts in water (**Scheme 1**), and the obtained solid was recrystallized in DMSO to get crystals suitable for X-Ray analysis. Compound **2** was obtained by using H_2F_4BDC instead of H_4DOBDC. The $[Yb_4(ClCNAn)_5(DOBDC)_1(DMSO)_{10}]_n.(DMSO)_2$ (**1**) and $[Yb_2(ClCNAn)_2(F_4\text{-}BDC)(DMSO)_6]_n$ compounds (**2**) are neutral polymeric 2D porous networks.~~

~~In order to gain deeper insight also into the photophysics of the linkers,~~ In order to deeply investigate the photophysics of the linkers, their dianionic forms have been prepared as $[Ph_4P]_2$[ClCNAn], $[Ph_4P]_2$[DOBDC] and $[Ph_4P]_2[F_4BDC]$ salts, ~~obtained~~ by reacting the monoprotonated KHClCNAn, H_4DOBDC and H_2F_4BDC, respectively, in water containing Ph4PBr salt in stoichiometric ratio (*vide supra*).

Scheme 1: ~~Schematic representation of~~ Description of the synthesis of compounds **1**-**2** and the corresponding nanosheets **1-NS** and **2-NS**.

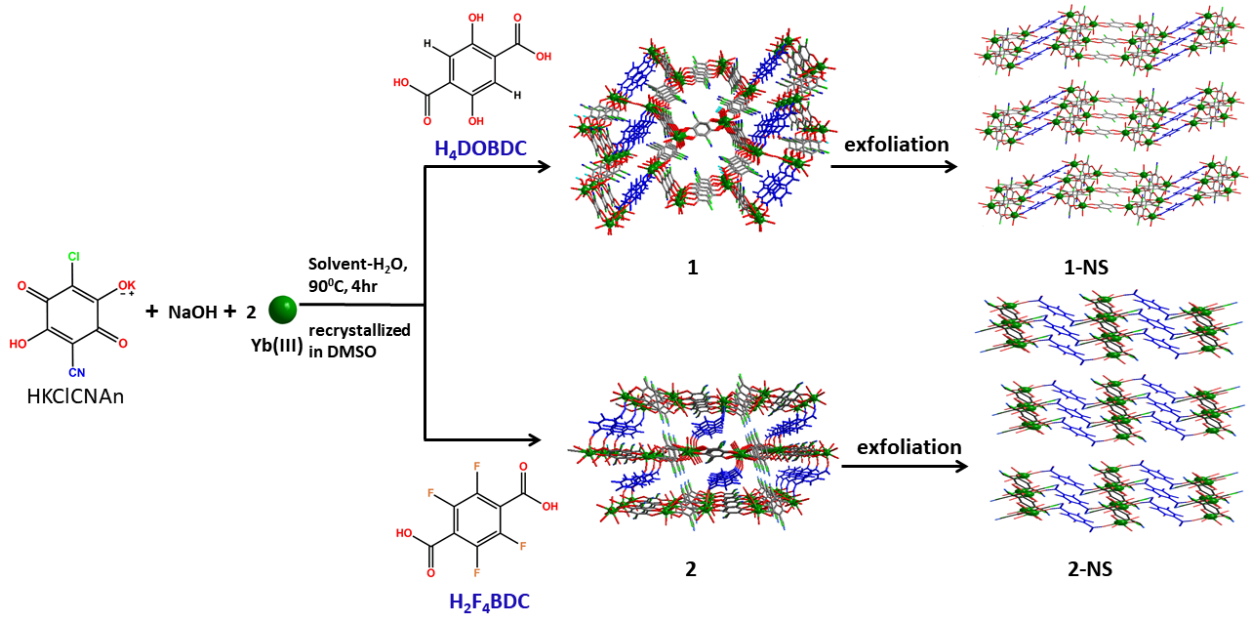

Crystal Structures.

Compounds **1-2** are 2D neutral porous CPs ~~formed by~~ built by Yb^{III} with $ClCNAn^{2-}$, $DOBDC^{2-}$ or F_4BDC^{2-} mixed ligands. Compound **1** crystallizes in the *P*-1 space group (triclinic) and the asymmetric unit ~~consists of~~ is formed by two Yb^{III} ions, two and half molecules of $ClCNAn^{2-}$ ligand, one half molecule of $DOBDC^{2-}$, five ~~coordinated~~ DMSO molecules ~~giving rise~~ producing a 2D network. ~~The coordination modes of~~ The two ligands $ClCNAn^{2-}$ and $DOBDC^{2-}$ coordinate Yb^{III} ions in different modes ~~are different~~. The $ClCNAn^{2-}$ ligands are coordinated to Yb^{III} in a bis-1,2 bidentate mode (Mode I), while the $DOBDC^{2-}$ are coordinated to Yb^{III} through a bis-monodentate mode (Mode II), as shown in Chart 1. Due to the inversion centre, in the anilate ligands the chloro and cyano substituents are disordered and equally distributed over two positions.

~~The~~ Coordination environments of the two independent Yb^{III} ions are different, depending on the ~~coordinated~~ ligand **(Figure 1a)**. Yb1 ion is coordinated to eight oxygen atoms, six from three $ClCNAn^{2-}$ ligands and two from ~~coordinated~~ DMSO molecules, resulting in distorted trigonal dodecahedron geometry **(Figure S1)**. Yb2 ion is coordinated to eight oxygen atoms, four from two $ClCNAn^{2-}$ ligands, one from the $DOBDC^{2-}$ ligand and three from ~~coordinated~~ DMSO molecules, overall forming a Yb1O8 coordination environment with a significantly distorted trigonal dodecahedron geometry. Yb−O bond lengths and O−Yb−O angles are in the range 2.238 (6)-2.363(6) Å and 66.6(2)−147.4(2)°, respectively.

In **1**, $Yb(ClCNAn)_n$ zig-zag 1D chains are formed by $ClCNAn^{2-}$ ligand bridging adjacent Yb1 and Yb2 along *b* axis **(Figure 1b, left side)**. $ClCNAn^{2-}$ and $DOBDC^{2-}$ ligands are alternatively linked to these 1D chains to give a 2D $Ln(ClCNAn)_n$ layer along the *bc* plane, forming

hexagonal cavities (noted as I) and rectangular cavities (noted as II) respectively. The layers are eclipsed along *a* axis**(Figure 1d).** Each Yb1 ion is connected to three other Yb1 ions through bis bidentate $ClCNAn^{2-}$ ligands forming (6,3)-2D topology six-membered rings with hexagonal cavities (cavity I). The different coordination mode of the $DOBDC^{2-}$ ~~gives rise to~~ produces larger rectangular cavities (cavity II) formed by six Yb^{III} ions, four $ClCNAn^{2-}$ and two $DOBDC^{2-}$ **(Figure 1b)**. In the *bc* plane, these cavities are alternatively arranged in the same layer. The coordinated DMSO molecules face towards the cavities and towards neighboring layers **(Figure 1c, S1b)**. This results in a ~~non-negligible~~ not insignificant overlap of the 2D layers and in ~~numerous~~ several interlayer interactions between the ~~DMSO molecules from one layer and the Yb^{III} centers from the neighboring layer~~ the Yb^{III} centers from one layer and the DMSO molecules from the neighboring layer **(Table S1)**. ~~According to SQUEEZE program,~~ The unit cell contains a void volume of 259 $Å^3$, containing *ca.* 74 electrons, which corresponds to approximately two DMSO molecules/formula unit, ~~molecules per formula unit~~ as calculated from SQUEEZE program. The DMSO solvent molecules are probably located in these two types of cavities **(Figure S2)**.

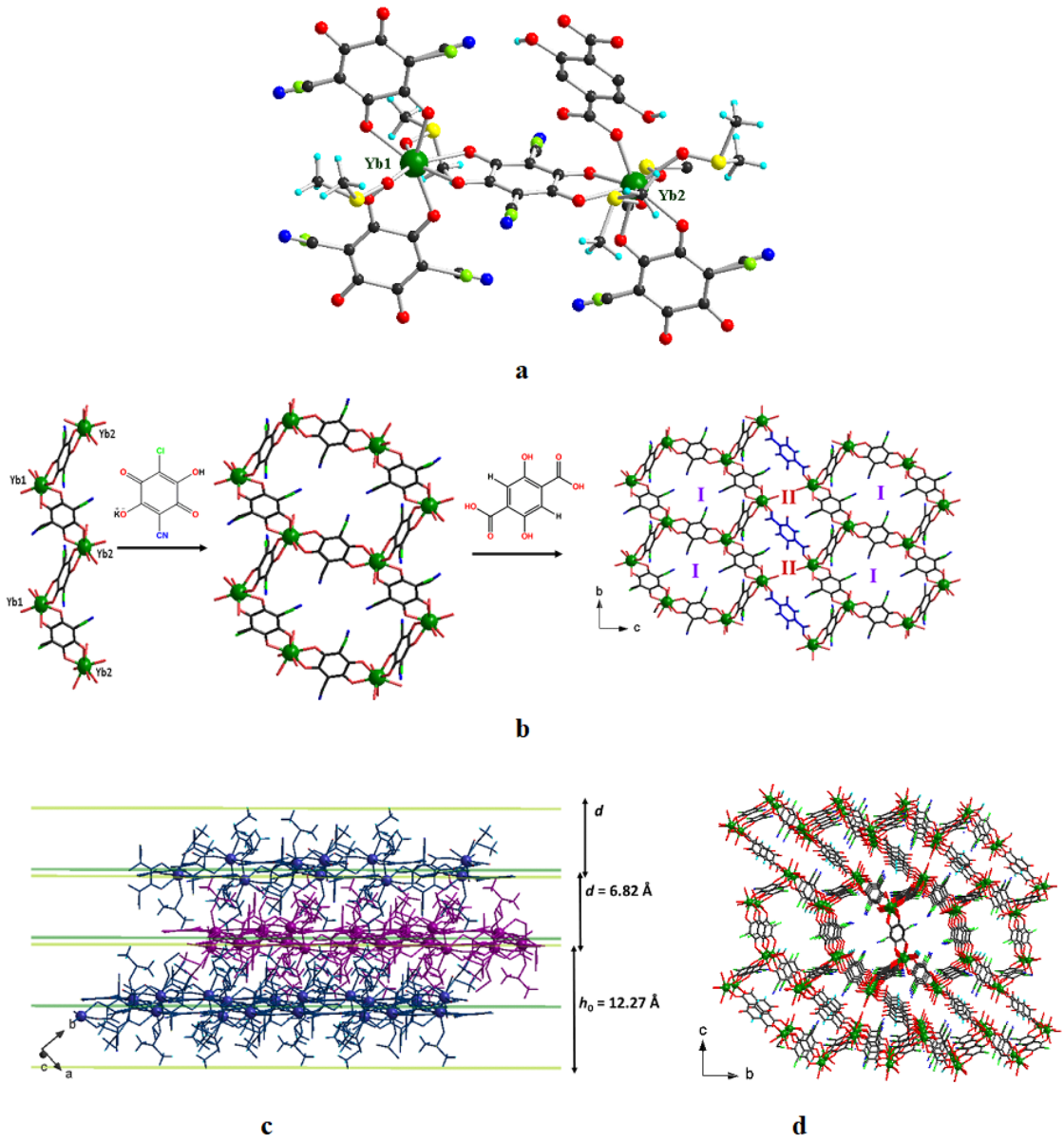

Figure 1. (**a**) ~~The~~ Coordination environment of Yb^{III} centers in **1**. (**b**) $Yb(ClCNAn)_n$ chain along *b* axis (left); 2D $Ln(ClCNAn)_n$ sheet along *bc* plane (middle); View of the final 2D layers in the *bc* plane ($DOBDC^{2-}$ is highlighted in blue (right)). (**c**) Height of a monolayer (*ho*) and interlayer distance (*d*) in three consecutive 2D layers. ~~View of three consecutive 2D layers showing the thickness of the first monolayer (*ho*) and interlayer distance (*d*).~~ (**d**) Perspective

view of **1** along *a* axis. Color code: Yb = green, O = red, Cl = light green, C = black, N = blue and H = cyan. In (b) and (d) DMSO solvent molecules are omitted for clarity reasons.

Compound **2** crystallizes in the triclinic *P*-1 space group and the asymmetric unit of **2** contains one Yb^{III} ion, two half molecules of $ClCNAn^{2-}$, one half molecule of F_4BDC^{2-} and three ~~coordinated~~ DMSO solvent molecules ~~giving rise~~ producing a 2D network of formula $[Yb_2(ClCNAn)_2(F_4BDC)_1(DMSO)_6]_n$ **(Figure 2a)**. The coordination mode of the two ligands is the same as in compound **1**. The $ClCNAn^{2-}$ ligand is coordinated in the bis-1,2 bidentate coordination mode while F_4BDC^{2-} is coordinated through bis-monodentate coordination mode **(Chart 1)**. The chloro and cyano substituents from the $ClCNAn^{2-}$ ligand are disordered and equally distributed over the two positions as in **1**.

Yb^{III} ion is coordinated to eight oxygen atoms, six from three $ClCNAn^{2-}$, one from F_4BDC^{2-} and three from DMSO molecules, showing distorted trigonal dodecahedron geometry **(Figure S3a)**. Yb−O bond lengths and O−Yb−O angles are in the range 2.191(7) − 2.418(7) Å and 65.5(2)−150.7(3)°, respectively. Yb^{III} ions are linked to $ClCNAn^{2-}$ ligands to generate infinite 1D chains along the *c* axis. These chains are linked to F_4BDC^{2-} ligands to finally form a 2D slanted grid-like layer with distorted square cavities ((6,3)-2D topology, **(Figure 2b)**. The 2D wave-like layers are eclipsed along the *a* axis **(Figure 2b, d)**.

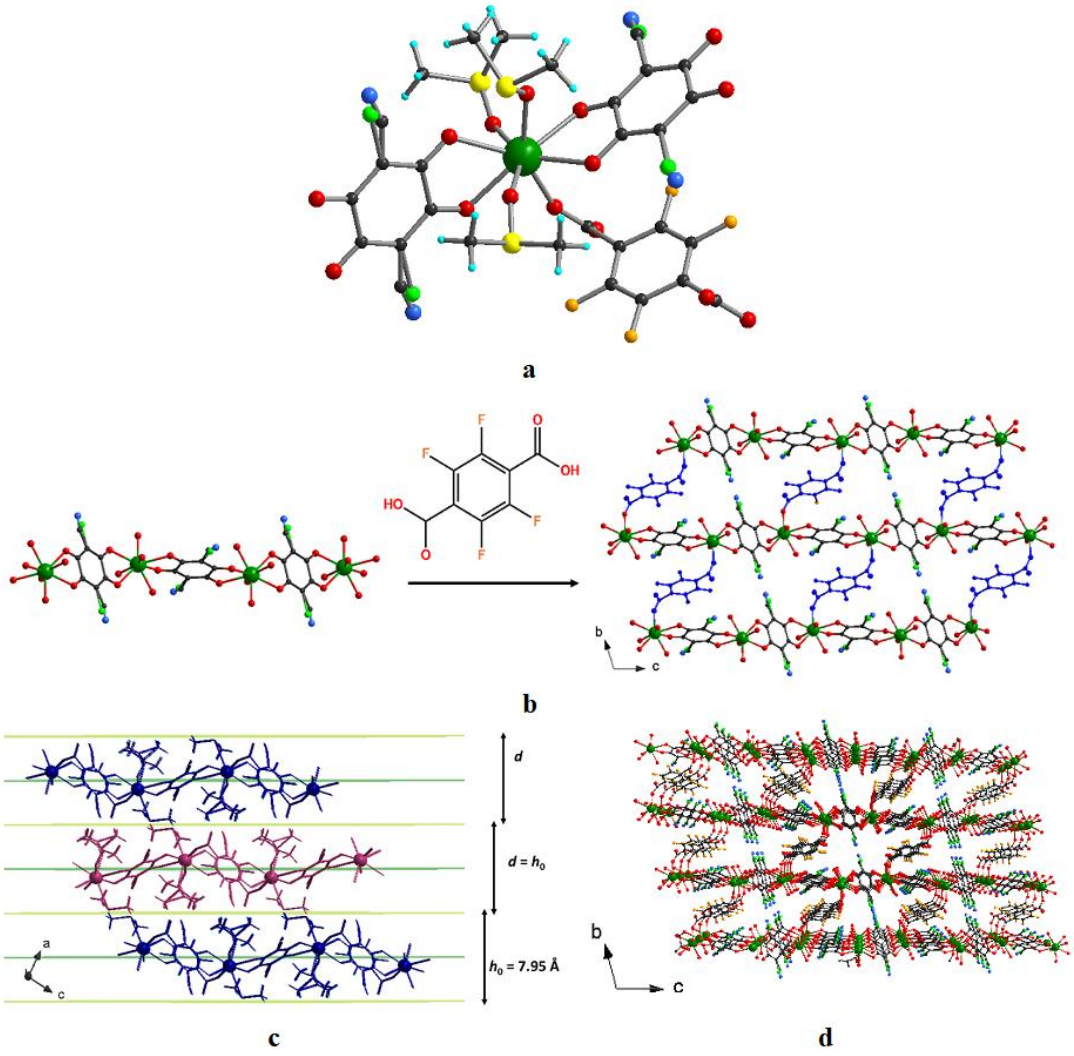

Figure 2. (**a**) ~~The~~ Coordination environment of Yb^{III} centers in **2**. (**b**) $[Yb(ClCNAn)]_n$ chain along the *c* axis (left); view of the 2D layers in the *bc* plane; F_4BDC^{2-} is highlighted in blue (right) (**c**) Height of a monolayer (*ho*) and interlayer distance (*d*) ~~view of~~ in three consecutive 2D layers in the *ac* plane. ~~showing the thickness of the first monolayer (*ho*) and interlayer distance (*d*).~~ (**d**) Perspective view along of **2** the *a* axis. Color code: Yb = green, O = red, Cl = light green, C = black, N = blue and H = cyan. In (b) and (d), DMSO molecules are omitted for clarity reasons.

Even though the Ln^{III} salt/$ClCNAn^{2-}$/carboxylate ~~ligand~~ stoichiometric ratio in the reaction is 2:1:1, the formula ratios are 2:2.5:0.5 for **1** and 2:2:1 for **2** respectively, indicating that the anilate ligand has a stronger affinity towards Ln^{III} than the carboxylate ~~ligand~~ one. A summary of crystallographic data for compounds **1-2** is reported in Table S2, Experimental Section, SI.

~~Despite the fact that~~ Although the coordination modes of $DOBDC^{2-}$ and F_4BDC^{2-} are the same, the shape of the 2D layers is different. In the case of $DOBDC^{2-}$, there are two crystallographically independent Yb^{III} ~~Ln^{III}~~ ions with different coordination geometries and therefore two types of cavities inside the 2D layer: hexagonal honeycomb cavities formed by Yb1 and $ClCNAn^{2-}$ and rectangular cavities formed by Yb2, $DODBC^{2-}$ and $ClCNAn^{2-}$. With F_4BDC^{2-}, there is only one independent Yb^{III} ion and one type of square cavity formed by Yb^{III}, F_4BDC^{2-} and $ClCNAn^{2-}$. The thickness of a monolayer (ho) and the interlayer distance (d) (**Figures 1c, 2c,** for compound **1** and **2**, respectively) can be calculated from the crystal structure[47] (see **Section S1** in SI). These parameters (ho and d) along with the Miller Indices of the exfoliation plane (Σ) of **1−2** compounds, are summarized in **Table 1.**

~~In compound **1**, the coordinated DMSO molecules are overlapped/interpenetrated with the neighbor layers, the overlapping interlayer distance has to be considered to determine the number of layers, taking into account from the thickness of the exfoliated sheets. The height of a monolayer (ho) and the interlayer distance (d) can be easily calculated from the crystal structure **(Figure 1c)**. The number of layers (n) of an exfoliated sheet 2D crystal slab of thickness h can thus be calculated as:~~

~~$$n = 1 + (h - ho)/d$$~~

~~However, in compound **2**, DMSO molecules are not overlapped like in compound **1 (Figure 2c)**. Hence, ho is equal to d, the number of layers (n) of an exfoliated sheet a 2D crystal slab of thickness h can thus be calculated as:~~

$$n = h/d$$

~~A summary of Miller Indices of the exfoliation plane (Σ), height of a monolayer (ho), and interlayer distance (d) of **1−2** layered compounds is reported in **Table 1.** for compounds **1−2**.~~ **(MOVE TO SI as Section 1)**

Table 1: Miller Indices of the exfoliation plane (Σ), monolayer thickness (ho) and interlayer distance (d) of **1−2** ~~layered~~ compounds.

Compound	∑	***ho***	***d***
1	1-11	12.27	6.82
2	-101	7.95	7.95

Synthesis and Morphological Characterization of 1-2 Nanosheets.

To confirm the formation of delaminated **1-2-NS**, AFM and HR-TEM measurements were carried out to examine their morphology. **3-NS** (Yb-Homoleptic CP nanosheets, *vide supra*) were also synthesized as reference. **1-3-NS** isopropanol suspensions were deposited on Si/SiO_2 substrates and were analyzed by AFM. AFM characterization of dropcast suspensions, obtained by crystal sonication, revealed the 2D nature of the compounds (**Figure 3**). Micrometer-sized

nanosheets were obtained with heights ranging from one to eight in number of layers (see **Table 1** and **Section S1**). Monolayer-thick portions of nanosheets were shown in **2-NS (Figure 3**b). ~~In **3-NS** reference, the interaction of the AFM tip with the nanosheets resulted in some degradation of their surface, which is clearly visible as the one-layer fluctuations in the height profiles depicted in **Figure 3**f, in agreement with previous findings on **3-NS**.~~[47]

TEM images show ~~confirm~~ the presence of very thin overlapped sheets for both **1-2-NS** samples (Figure 4, a-b). ~~The contrast of the TEM images indicates that the layers are very thin~~. High resolution images for **1-2-NS** are reported in Figure 4 along with the reference **3-NS** (Figure 4c-f). Well defined lattice fringes with interplanar average distances of, and 3.0 Å, 2.6 Å and 1.8 Å, were observed for both compounds which can be ascribed to the reticular planes (3 0 0) at 2.98 Å, (0 6 0) at 1.80 Å and (-3 2 0) at 2.6 Å for **1** and (1 -3 3) at 2.98 Å and (2 3 3) at 1.80 Å for **2**, as shown in Figures S4 and S5. Crystalline nanodomains with different orientations can be observed showing that the 2D sheets are made of multi-nanodomain crystalline structure. It is worth noting the excellent stability of **1-2 NS** under electron beam irradiation over time, as already highlighted in the AFM images (*vide supra*), which makes them reliable nanoplatforms for advanced photophysical studies. Heteroleptic **1-2-NS** are the most robust and reliable nanoplatforms in the anilato-based CPs/MOFs, even when compared with the **3-NS** homoleptic ones.[47,54,55] Lattice fringes are rarely observed in MOF-based nanosheets[56–58], due to their instability under the irradiation exposure.

The successful delamination of **1-2** CPs to obtain **1-2 NS** was further confirmed for both samples by powder x-ray diffraction (PXRD of nanosheets, bulk and theoretical patterns, calculated by CIF data are reported in Figure S6) as the diffraction peaks associated with the exfoliation plane (*i.e.* 1-11 and -101 for compound **1** and **2**, respectively), was found to

significantly decrease or disappear in the NS PXRD patterns, compared to the bulk ones. Furthermore **1-2 NS** PXRD showed that the crystallinity of the bulk CPs was preserved after the exfoliation, but generally with peaks of lower intensity in the nanosheet patterns than the bulk ones.

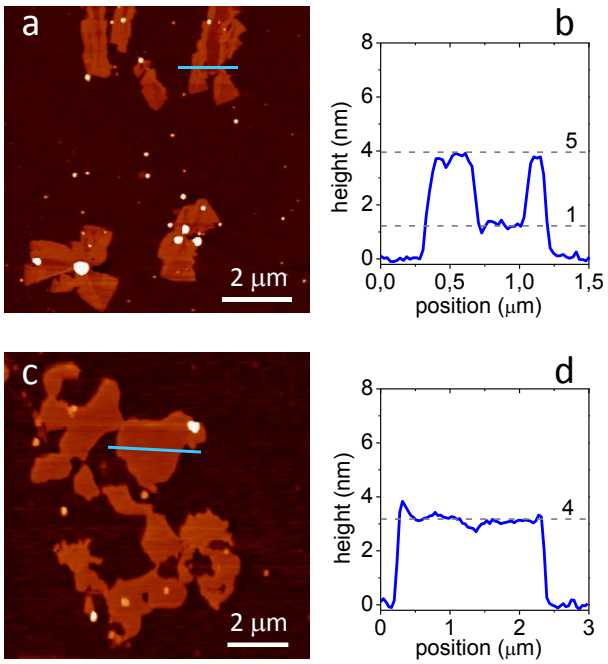

Figure 3. AFM characterization of dropcast nanosheets of compounds **1-3**. (a) Height image of **1-NS**; (b) Height profile of **1-NS** along the line depicted in panel (a). (c, d) Same as in panels a,b but for **2-NS**. ~~(e, f) Same as in panels a, b but for **3-NS**.~~ Numbered dashed lines ~~in panels b and d,and f~~ mark the heights of the corresponding numbers of layers.

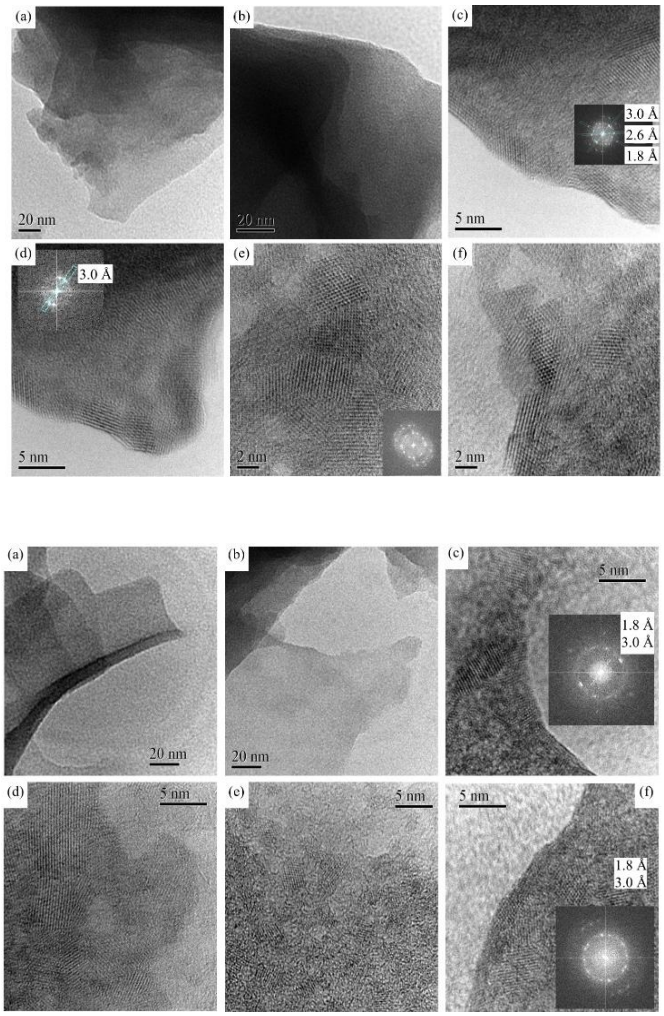

Figure 4. TEM (a,b) and HR-TEM (c-f) of ~~the sample~~ **1-NS** (top) and **2-NS** (bottom).

Photophysical Studies

a. Intrinsic photophysical properties of bulky sized 1-2. Diffuse reflectance measurements revealed broadband absorption across the 350-750nm spectral range in crystals of **1-2**(**Figure 5**a) which was ascribed mainly to ligand-centered absorption in the$ClCNAn^{2-}$ ligand. At the wavelength used for PL excitation (355nm), both $ClCNAn^{2-}$ and $DODBC^{2-}$ ligands appeared to contribute to photoabsorption in **1**, whereas F_4BDC^{2-} play a negligible role in the photoexcitation of **2**. As shown in **Figure 5**b, clear evidence of resonant absorption from Yb^{3+} ions was collected

in crystals of both **1** and **2**. PL studies revealed a weak ligand-centered emission extending from 650 to beyond 900 nm, which was traced back to the $ClCNAn^{2-}$ ligand in the presence of solid-state effects, causinga sizeable redshift of the emission. This attribution resulted from the parallel analysis of crystals of $[Ph_4P]_2[DOBDC]$, $[Ph_4P]_2[F_4BDC]$, and $[Ph_4P]_2[ClCNAn]$, where the role of the dianionic ligands could be singled out. Some evidence of efficient Yb^{3+} emission sensitization by photoexcited ligands (antenna effect)[59] was provided by the fact that lanthanide-centered emission dominate over the ligand-centered emission in both heteroleptic compounds, as can be easily deduced from the Vis/NIR signal amplitudes (**Figure 5**c,d). As a result of the much smaller quantity of material investigated in the nanosheet suspensions, PL signals collected in **1-2-NS** were considerably lower than those of the corresponding crystals.

Transient PL studies showed that the ligand-centered emission is very short lived (< 30 ps, resolution limited) in both compounds **1-2** (**Figure 5**e), whereas in the Ph_4P salts the dianionic ligands exhibit relatively long PL lifetimes ranging in the nanosecond time scale (**Figure 5**f). These findings were ascribed to the heavy-atom effect ~~induced~~ due to ~~the~~ lanthanide ions, leading to heavy-atom effect/ultrafast intersystem crossing (ISC).[60]Last, NIR PL decay transients at ~1 μm wavelength revealed nearly monoexponential decays of sensitized Yb^{III} ions with characteristic times of a few microseconds in both compounds **1-2 (Figure 5**g). Microsecond PL lifetimes were partly ascribed to vibrational quenching of the lanthanide emission acted by the C-H groups of the coordinated DMSO molecules. It was not possible to single out the contribution of DMSO molecules to the lanthanide nonradiative decay due to the lack of an isostructural CP where DMSO molecules is replaced by another solvent not bearing C-H groups. Besides, theoretical studies of vibrational quenching by DMSO molecules are still unavailable. Multiexponential decays with shorter average lifetimes were found in the corresponding

nanosheet suspensions, which could be attributed (i) to an increase in lanthanide non radiative recombination centers within the crystal structure as a result of the exfoliation process, and (ii) to solvent-related additional vibrational quenching of the lanthanide emission, as previously discussed for **3-NS**.[59,61–64]

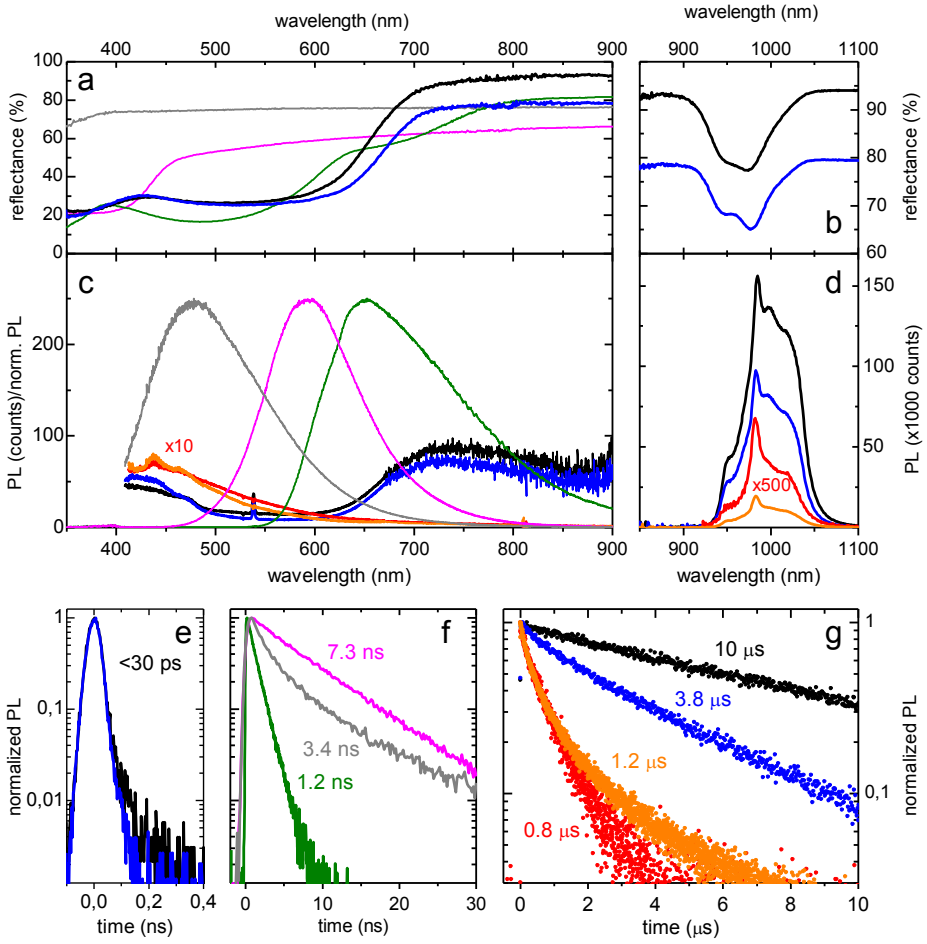

Figure 5. Optical and photophysical characterization of crystals of compounds **1 (**black lines/dots) and **2** (blue lines/dots)**,** and ethanol isopropanol suspensions of **1-NS** (red lines/dots) and **2-NS** (orange lines/dots); reference data on crystals of $[Ph_4P]_2$DOBDC (magenta lines), $[Ph_4P]_2F_4$BDC (grey lines), and $[Ph_4P]_2$[ClCNAn](green lines) are also shown. (a) Diffuse (hemispherical) reflectance spectra across a broad Vis-NIR spectral range. (b) Diffuse

reflectance spectra across the Yb^{3+} absorption/emission spectral range. (c) PL spectra across the same spectral range as in (a). (d) PL spectra across the same spectral range as in (b). (e, f) Ligand-centered PL decay profiles. (g) Lanthanide-centered NIR-PL decay profiles. Average lifetimes obtained from multiexponential fit curves are indicated.

b. Advanced 1-2-NS photophysics. Deeper insight into the **1-2-NS** photophysics could be gained by perturbing their isopropanol suspensions *via* addition of small quantities of aliphatic and aromatic solvents (CH_3CN, CH_3NO_2, $C_6H_5NH_2$, $C_6H_5CH_3$, $C_6H_5NO_2$, C_6H_5CN). Among aromatic solvents, electron-withdrawing (-CN, $-NO_2$) and electron-donating groups ($-CH_3$, $-NH_2$) in the benzene ring were selected. Here, the photophysical response of the nanosheets was analyzed using a PL multiprobe approach under pulsed photoexcitation, where not only the integrated PL signal (i.e., $\int_0^\infty \mathrm{PL}(t)dt$) was used as optical probe, but also the initial PL signal ($\mathrm{PL}_0 = \mathrm{PL}(0)$) and the PL lifetime $\tau = \int_0^\infty \mathrm{PL}(t)dt/\mathrm{PL}_0$. For a multiexponential decay function, τ coincides with the amplitude-weighted average of the characteristics times of the single exponential components (see Experimental Section). In fact, the overall PL quantum yield of the Ln^{III} coordination compounds can be written ad $\mathrm{QY} = \eta_s \mathrm{QY}_i$, where η_s is the lanthanide sensitization efficiency andQY_i is the intrinsic lanthanide PL quantum yield. If the activation time of the NIR PL signal of the lanthanide ions is much faster than its decay time, which is very much often the case, as in these compounds (**Figure 5**g), the initial PL signal amplitude, PL_0, is proportional to η_s, whereas the PL lifetime $\tau$is always proportional to QY_i. Hence, a variation in PL_0 and τ can be traced back to a perturbation produced, respectively, in the lanthanide emission

quenching and in the antenna effect, hence making the multiparameter analysis of the PL response an effective probe of multiple photophysical processes.

As clearly visible in **Figure 6 a-c**, addition of various solvents at 1% v/v concentration produced little or no variation in any of the PL parameters, exception made for nitrobenzene, to which the nanosheet suspensions reacted with a reduction in PL_0 and, simultaneously, in the integrated PL signal. The very weak response observed in τ was readily interpreted as a negligible sensitivity of vibrational quenching of the Yb^{III} emission to small changes in solvent composition. This is reasonable since the addition of small quantities of different solvents (that is, the analytes) produces only a little variation in the density of vibrational oscillators in the medium surrounding the Yb^{3+} ions.[61] A sizeable reduction in PL_0 was observed in both heteroleptic compounds **1-2-NS** and in the homoleptic one (**3-NS**) and could therefore be traced back to a specific excited-state interaction between nitrobenzene and the $ClCNAn^{2-}$ ligand.

The interaction mechanism was assigned to photoinduced charge-transfer (PCT)[65] from the $ClCNAn^{2-}$ ligand to nitrobenzene. Owing to the strong electron-withdrawing power of the -NO2 group, nitrobenzene is more electron-deficient than the $ClCNAn^{2-}$ ligand; this results in an electronic level alignment where the lowest unoccupied molecular orbital (LUMO) of $ClCNAn^{2-}$ ~~lies~~ has higher ~~in~~ energy than the LUMO of nitrobenzene, hence so enabling PCT from $ClCNAn^{2-}$ (photoexcited electron donor) to nitrobenzene (electron acceptor),with consequent loss in Yb^{III} emission sensitization efficiency and reduction inPL_0.[65]This interaction mechanism has in fact been widely used in the fluorescence turn-off detection of electron–deficient analytes using fluorescent MOFs.[66] It is worth noting that, for fluorescence turn-off to occur with high sensitivity, PCT towards the analyte must be much faster than the ISC process occurring within

the CP itself. This is clearly a challenging task as the heavy-atom effect ~~induced by~~ due to the lanthanide greatly accelerates ISC.

~~In order~~ To evaluate the sensitivity of the PL turn-off process, nitrobenzene titration curves were measured for suspensions of **1-2-NS (Figure 6d-f)**. Reference titration curve was produced for a suspension of **3-NS** to assess the role of the $ClCNAn^{2-}$as sole ligand. Increasing the nitrobenzene concentration resulted in a progressive reduction in PL_0 and integrated PL in all compounds; only a negligible effect was found on τ for analyte concentrations as large as 4%v/v. Titration curves were fitted with a single exponential decay function $\%p = 100\% \cdot \exp[-c/c_0]$, where %p represents the signal percentage amplitude, c is the nitrobenzene concentration and c_0 is the characteristic concentration of the decay. This analysis yielded $c_0 \sim 1\%$ v/v, or equivalently, low-concentration sensitivities $(-100\%/c_0)$ of ca. -100%p/(% v/v). As mentioned before, this moderate sensitivity was ascribed to the ultrafast ISC process at the basis of antenna effect towards the Yb^{III} ions.

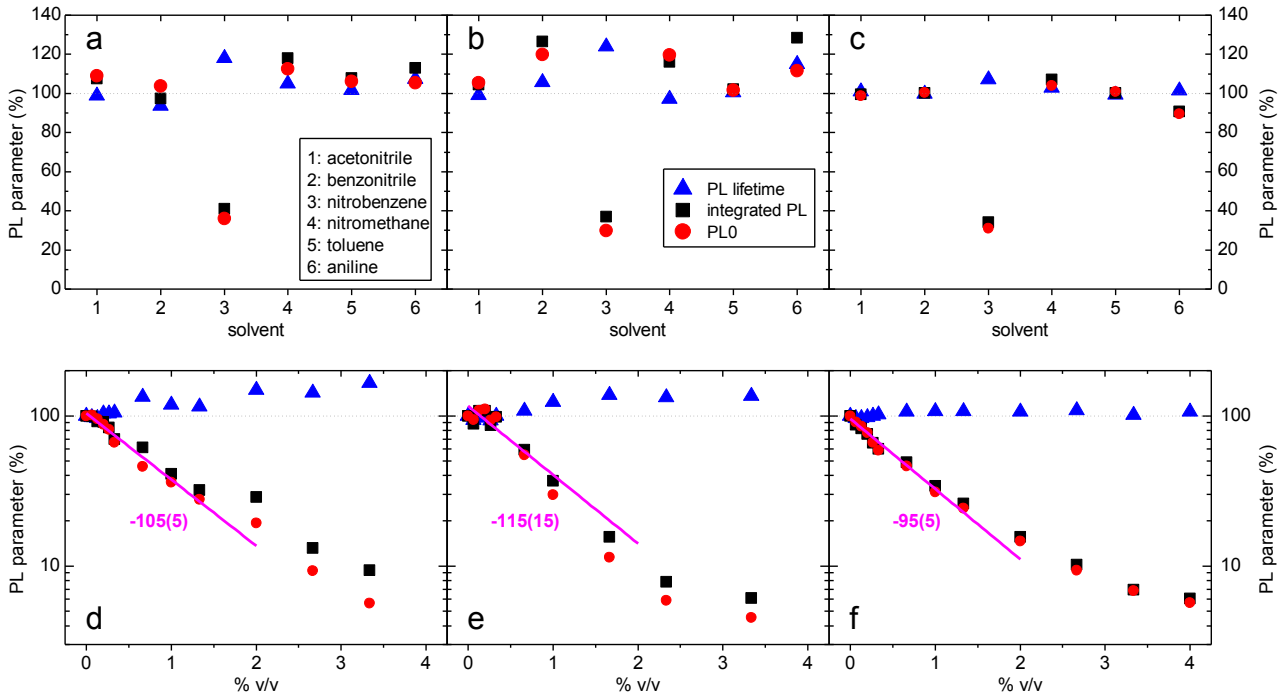

Figure 6. Multiprobe photoluminescence studies on isopropanol suspensions of **1-3-NS**. (a) Percentage values of PL parameters (PL lifetime, time-integrated PL, and PL_0 = initial PL) uponaddition of different solvents (1% v/v) to a **1-NS** suspension. (b) Same as in (a) but for a **2-NS** suspension. (c) Sample as in (a) but for a **3-NS** suspension. Dashed horizontal lines in panels (a-c) mark the 100% reference value. Solvent legend and PL parameter legend apply to all panels. (d) Percentage values of PL parameters (% p) versus percentage quantity of nitrobenzene added to a**1-NS** suspension (% v/v). Magenta lines: best exponential decay fits to PL_0 data with indication of characteristic sensitivity in%p/ (% v/v) units (2σ errors). (e) Same ad (d) but for a **2-NS** suspension. (f) Same as (d) but for a **3-NS** suspension.

Remarkably, the homoleptic **3-NS** displays almost the same sensitivity to nitrobenzene as the heteroleptic **1-2-NS**, allowing us to infer that the $ClCNAn^{2-}$ ligand plays a dominant role in the Yb^{III} sensitization In **1-NS**, where the $DOBDC^{2-}$ and $ClCNAn^{2-}$ ligands seem to compete against

each other in absorbing the 355-nm laser pump light (**Figure 5**a), this result hints to an unfavorable energy level alignment between the triplet state of $DOBDC^{2-}$ and the $^2F_{5/2}$ energy level of Yb^{3+}, resulting in inefficient ligand-to-~~metal~~ lanthanide energy transfer. Besides, the lack of Yb^{III} emission sensitization by the F_4BDC^{2-} ligand in **2-NS** could be easily understood as a consequence of the large singlet and triplet energies of F_4BDC^{2-} (>34000 and >27000 cm^{-1}, respectively),[67] making both photoabsorption and energy-transfer towards the lanthanide not efficient processes.

EXPERIMENTAL SECTION has been moved to SUPPLEMENTARY INFORMATIONS

Conclusions

Novel robust and crystalline 2D nanosheets of novel heteroleptic2D layered NIR emissive lanthanide MOFs/CPs $[Yb_4(ClCNAn)_5(DOBDC)_1(DMSO)_{10}]_n.(DMSO)_2$ (**1**) and $[Yb_2(ClCNAn)_2(F_4BDC)(DMSO)_6]_n$ (**2**)($ClCNAn^{2-}$= 3-chloro-6-cyano-anilate, $DOBDC^{2-}$ = 2,5-dihydroxy benzene-1,4-dicarboxylate F_4BDC^{2-} = 2,3,5,6-tetrafluorobenzene-1,4-dicarboxylate) were successfully obtained.The synthesis and structural characterization of the bulky sized corresponding 2D neutral CPs, with a special emphasis on the lanthanide coordination environment,exfoliation planes and distances between them being clearly identified, were also reported,**1-2**representing the first examples of heteroleptic lanthanide MOFs/CPs based on anilate and carboxylate ligands. **1-2-NS** were fabricated by successful exfoliation of **1-2** bulky sized CPs down to few monolayers and lateral micrometric size have been observed by AFM,

while PXRD and HR-TEM measurements clearly showed the preservation of crystallinity upon exfoliation, an indication of the robustness of the 2D nanosheets.

Conventional photophysical studies on both bulk and nanosheets have been undertaken, highlighting the antenna effect of the heterosubstituted anilate linker and the downsizing effect on the lifetime of the decay process. Due to their robustness, the 2D nanosheets are ideal nanoplatforms to perform advanced photophysical studies by an innovative multiprobe approach, based on the study of small perturbation of lifetime, photoluminescence (PL) and integrate PL, induced by different solvents, both aromatic and aliphatic, bearing electro-withdrawing and electro-donating groups. PL turn-off towards nitrobenzene was observed which can be understood in terms of very efficient ISC process from the anilate to the Yb^{III} center compared to the competitive PCT process from the anilate to nitrobenzene. It is envisaged that the PL turn-off sensitivity could be greatly improved by resorting to CPs bearing electron-rich linkers. In conclusion, these results contribute to the development of research on 2D nanosheets nanomaterials, in particular they show how to design and fabricate robust and crystalline nanosheets and simultaneously give a roadmap, based on advanced multiprobe photophysical studies, towards challenging applications, such as the design of prototype nanoplatforms for sensing and detection of explosives as TNT or picric acid, which represent a philanthropic task of paramount importance for homeland security.

AUTHOR INFORMATION

Corresponding Author

*E-mail: mercuri@unica.it. Fax: (+39)0706754474. Phone:(+39)0706754856.

*E-mail: narcis.avarvari@univ-angers.fr. Fax: (+33)02 41 73 5405. Phone: (+33)02 41 73 50 84.

*E-mail: francesco.quochi@dsf.unica.it. Fax: (+39)0706753191. Phone: (+39)0706754866

Conflicts of interest

There are no conflicts to declare.

Author Contributions

Funding Sources

This work was supported in Italy by the Fondazione di Sardegna-Convenzione triennale tra la Fondazione di Sardegna e gli Atenei Sardi, Regione Sardegna-L.R. 7/2007 annualità 2016-DGR 28/21 del 17.05.2015 "Innovative Molecular Functional Materials for Environmental and Biomedical Applications", ~~and~~ INSTM and "SULCIS 820889". "SULCIS 820947" "SENSORI LUMINESCENTI AD EFFETTO PLASMONICO PER IL RILEVAMENTO DEI METALLI PESANTI NELLE ACQUE", REGIONE AUTONOMA DELLA SARDEGNA, is also acknowledged for grant to ~~Suchithra Ashoka Sahadevan~~ S.A.S. ~~researeh grant~~. The work in France was supported by the University of Angers, the CNRS and the RFI Regional project LUMOMAT (grant to A.A., Project ASCO MMM).

Notes

Crystallographic data for the structures were deposited in the Cambridge Crystallographic Data Centre, deposition numbers 1944824-1944825. These data can be obtained free of charge from The Cambridge Crystallographic Data Centre via www. ccdc.cam.ac.uk/data_request/cif.

ACKNOWLEDGMENT

The authors ~~acknowledge~~ are greatful to Centro Servizi d' Ateneo per la Ricerca, CeSAR, ~~(Centro Servizi d' Ateneo per la Ricerca)~~, core facility of the University of Cagliari, for ~~the use of~~ using the Ultrafast Optical Spectroscopy Laboratory for photophysical measurements and the JEM 2010 UHR JEOL ~~facility~~ Laboratory for TEM measurements.

ABBREVIATIONS

CP Coordination Polymer, MOF Metal Organic Framework, PL Photoluminescence, ISC Inter System Crossing, PCT photoinduced charge-transfer.

REFERENCES

(1) Furukawa, H.; Cordova, K. E.; O'Keeffe, M.; Yaghi, O. M. The Chemistry and Applications of Metal-Organic Frameworks. *Science.* **2013**, *341*, 1230444-1–12. https://doi.org/10.1126/science.1230444.

(2) Wang, C.; Liu, D.; Lin, W. Metal-Organic Frameworks as a Tunable Platform for Designing Functional Molecular Materials. *J. Am. Chem. Soc.* **2013**, *135*, 13222–13234. https://doi.org/10.1021/ja308229p.

(3) Lee, K.; Isley, W. C.; Dzubak, A. L.; Verma, P.; Stoneburner, S. J.; Lin, L. C.; Howe, J. D.; Bloch, E. D.; Reed, D. A.; Hudson, M. R.; Brown, C. M.; Long, J. R.; Neaton, J. B.; Smit, B.; Cramer, C. J.; Truhlar, D. G.; Gagliardi, L.Design of a Metal-Organic Framework with Enhanced Back Bonding for Separation of N_2 and CH_4. *J. Am. Chem. Soc.* **2014**, *136*, 698–704. https://doi.org/10.1021/ja4102979.

(4) Barea, E.; Montoro, C.; Navarro, J. A. R. Toxic Gas Removal – Metal–Organic Frameworks for the Capture and Degradation of Toxic Gases and Vapours. *Chem. Soc. Rev.* **2014**, *43*, 5419–5430. https://doi.org/10.1039/C3CS60475F.

(5) Nandasiri, M. I.; Jambovane, S. R.; McGrail, B. P.; Schaef, H. T.; Nune, S. K. Adsorption, Separation, and Catalytic Properties of Densified Metal-Organic Frameworks. *Coord. Chem. Rev.* **2016**, *311*, 38–52. https://doi.org/10.1016/j.ccr.2015.12.004.

(6) Horcajada, P.; Gref, R.; Baati, T.; Allan, P. K.; Maurin, G.; Couvreur, P.; Férey, G.; Morris, R. E.; Serre, C. Metal-Organic Frameworks in Biomedicine. *Chem. Rev.***2012**, *112*, 1232–1268. https://doi.org/10.1021/cr200256v.

(7) Li, H.; Eddaoudi, M.; O'Keeffe, M.; Yaghi, O. M. Design and Synthesis of an Exceptionally Stable and Highly Porous Metal- Organic Framework. *Nature* **1999**, *402*, 276–279. https://doi.org/10.1038/46248.

(8) Serre, C.; Millange, F.; Thouvenot, C.; Noguès, M.; Marsolier, G.; Louër, D.; Férey, G. Very Large Breathing Effect in the First Nanoporous Chromium(III)-Based Solids: MIL-53 or $Cr^{III}(OH)\cdot\{O_2C{-}C_6H_4{-}CO_2\}\cdot\{HO_2C{-}C_6H_4{-}CO_2H\}_x\cdot H_2O_y$. *J. Am. Chem. Soc.* **2002**, *124*, 13519–13526. https://doi.org/10.1021/ja0276974.

(9) Llewellyn, P. L.; Bourrelly, S.; Serre, C.; Filinchuk, Y.; Férey, G. How Hydration Drastically Improves Adsorption Selectivity for CO_2over CH_4in the Flexible Chromium Terephthalate MIL-53. *Angew. Chemie - Int. Ed.* **2006**, *45*, 7751–7754. https://doi.org/10.1002/anie.200602278.

(10) Latroche, M.; Surblé, S.; Serre, C.; Mellot-Draznieks, C.; Llewellyn, P. L.; Lee, J. H.;

Chang, J. S.; Sung, H. J.; Férey, G. Hydrogen Storage in the Giant-Pore Metal-Organic Frameworks MIL-100 and MIL-101. *Angew. Chemie - Int. Ed.* **2006**, *45*, 8227–8231. https://doi.org/10.1002/anie.200600105.

(11) Jeremias, F.; Khutia, A.; Henninger, S. K.; Janiak, C. MIL-100(Al, Fe) as Water Adsorbents for Heat Transformation Purposes—a Promising Application. *J. Mater. Chem.* **2012**, *22*, 10148–10151. https://doi.org/10.1039/C2JM15615F.

(12) Kapelewski, M. T.; Geier, S. J.; Hudson, M. R.; Stück, D.; Mason, J. A.; Nelson, J. N.; Xiao, D. J.; Hulvey, Z.; Gilmour, E.; Fitzgerald, S. A.; Head-Gordon, M.; Brown, C. M.; Long, J. R. M_2(m-DOBDC) (M = Mg, Mn, Fe, Co, Ni) Metal-Organic Frameworks Exhibiting Increased Charge Density and Enhanced H_2 Binding at the Open Metal Sites. *J. Am. Chem. Soc.* **2014**, *136*, 12119–12129. https://doi.org/10.1021/ja506230r.

(13) Zhang, H.; Zhou, L.; Wei, J.; Li, Z.; Lin, P.; Du, S. Highly Luminescent and Thermostable Lanthanide-Carboxylate Framework Materials with Helical Configurations. *J. Mater. Chem.* **2012**, *22*, 21210–21217. https://doi.org/10.1039/c2jm34088g.

(14) Allendorf, M. D.; Bauer, C. A.; Bhakta, R. K.; Houk, R. J. T. Luminescent Metal-Organic Frameworks. *Chem. Soc. Rev.* **2009**, *38*, 1330–1352. https://doi.org/10.1039/b802352m.

(15) Nayak, S.; Nayek, H. P.; Pietzonka, C.; Novitchi, G.; Dehnen, S. A Series of Three-Dimensional Lanthanide MOFs: Observation of Reversible Structural Changes Controlled by Solvent Desorption-Adsorption, and Magnetic Properties. *J. Mol. Struct.* **2011**, *1004*, 82–87. https://doi.org/10.1016/j.molstruc.2011.07.032.

(16) Bünzli, J. C. G.; Piguet, C. Lanthanide-Containing Molecular and Supramolecular

Polymetallic Functional Assemblies. *Chem. Rev.* **2002**, *102*, 1897–1928. https://doi.org/10.1021/cr010299j.

(17) Kuriki, K.; Koike, Y.; Okamoto, Y. Plastic Optical Fiber Lasers and Amplifiers Containing Lanthanide Complexes. *Chem. Rev.* **2002**, *102*, 2347–2356. https://doi.org/10.1021/cr010309g.

(18) Liu, W.; Huang, X.; Chen, C.; Xu, C.; Ma, J.; Yang, L.; Wang, W.; Dou, W.; Liu, W. Function-Oriented: The Construction of Lanthanide MOF Luminescent Sensors Containing Dual-Function Urea Hydrogen-Bond Sites for Efficient Detection of Picric Acid. *Chem. Eur. J.* **2019**, *25*, 1090–1097. https://doi.org/10.1002/chem.201805080.

(19) Bünzli, J.-C. G. Lanthanide Luminescence for Biomedical Analyses and Imaging. *Chem. Rev.* **2010**, *110*, 2729–2755. https://doi.org/10.1021/cr900362e.

(20) Rocha, J.; Brites, C. D. S.; Carlos, L. D. Lanthanide Organic Framework Luminescent Thermometers. *Chem. Eur. J.* **2016**, *22*, 14782–14795. https://doi.org/10.1002/chem.201600860.

(21) Yang, C.; Wang, X.; Omary, M. A. Fluorous Metal-Organic Frameworks for High-Density Gas Adsorption. *J. Am. Chem. Soc.* **2007**, *129*, 15454–15455. https://doi.org/10.1021/ja0775265.

(22) Yang, C.; Wang, X.; Omary, M. A. Crystallographic Observation of Dynamic Gas Adsorption Sites and Thermal Expansion in a Breathable Fluorous Metal-Organic Framework. *Angew. Chemie - Int. Ed.* **2009**, *48*, 2500–2505. https://doi.org/10.1002/anie.200804739.

(23) Hulvey, Z.; Sava, D. A.; Eckert, J.; Cheetham, A. K. Hydrogen Storage in a Highly Interpenetrated and Partially Fluorinated Metal-Organic Framework. *Inorg. Chem.* **2011**, *50*, 403–405. https://doi.org/10.1021/ic101153c.

(24) Zhang, D. S.; Chang, Z.; Li, Y. F.; Jiang, Z. Y.; Xuan, Z. H.; Zhang, Y. H.; Li, J. R.; Chen, Q.; Hu, T. L.; Bu, X. H. Fluorous Metal-Organic Frameworks with Enhanced Stability and High H_2/CO_2 Storage Capacities. *Sci. Rep.* **2013**, *3*, 1–7. https://doi.org/10.1038/srep03312.

(25) Chen, B.; Yang, Y.; Zapata, F.; Qian, G.; Luo, Y.; Zhang, J.; Lobkovsky, E. B. Enhanced Near-Infrared-Luminescence in an Erbium Tetrafluoroterephthalate Framework. *Inorg. Chem.* **2006**, *45*, 8882–8886. https://doi.org/10.1021/ic060568u.

(26) Han, Y.; Yan, P.; Sun, J.; An, G.; Yao, X.; Li, Y.; Li, G. Luminescence and White-Light Emitting Luminescent Sensor of Tetrafluoroterephthalate-Lanthanide Metal-Organic Frameworks. *Dalt. Trans.* **2017**, *46*, 4642–4653. https://doi.org/10.1039/c7dt00215g.

(27) Sobieray, M.; Gode, J.; Seidel, C.; Poß, M.; Feldmann, C.; Ruschewitz, U. Bright Luminescence in Lanthanide Coordination Polymers with Tetrafluoroterephthalate as a Bridging Ligand. *Dalt. Trans.* **2015**, *44*, 6249–6259. https://doi.org/10.1039/c4dt03733b.

(28) Atzori, M.; Pop, F.; Cauchy, T.; Mercuri, M. L.; Avarvari, N. Thiophene-Benzoquinones: Synthesis, Crystal Structures and Preliminary Coordination Chemistry of Derived Anilate Ligands. *Org. Biomol. Chem.* **2014**, *12*, 8752–8763. https://doi.org/10.1039/c4ob01582g.

(29) Atzori, M.; Artizzu, F.; Sessini, E.; Marchiò, L.; Loche, D.; Serpe, A.; Deplano, P.; Concas, G.; Pop, F.; Avarvari, N.; Mercuri, M. L. Halogen-Bonding in a New Family of

Tris(Haloanilato)Metallate(III) Magnetic Molecular Building Blocks. *Dalton Trans.* **2014**, *43*, 7006–7019. https://doi.org/10.1039/c4dt00127c.

(30) Atzori, M.; Marchiò, L.; Clérac, R.; Serpe, A.; Deplano, P.; Avarvari, N.; Mercuri, M. L. Hydrogen-Bonded Supramolecular Architectures Based on Tris(Hydranilato)Metallate(III) (M = Fe, Cr) Metallotectons. *Cryst. Growth Des.* **2014**, *14*, 5938–5948. https://doi.org/10.1021/cg501143z.

(31) Atzori, M.; Artizzu, F.; Marchiò, L.; Loche, D.; Caneschi, A.; Serpe, A.; Deplano, P.; Avarvari, N.; Mercuri, M. L. Switching-on Luminescence in Anilate-Based Molecular Materials. *Dalt. Trans.* **2015**, *44*, 15786–15802. https://doi.org/10.1039/C5DT02241J.

(32) Atzori, M.; Pop, F.; Auban-Senzier, P.; Gómez-García, C. J.; Canadell, E.; Artizzu, F.; Serpe, A.; Deplano, P.; Avarvari, N.; Mercuri, M. L. Structural Diversity and Physical Properties of Paramagnetic Molecular Conductors Based on Bis(Ethylenedithio)Tetrathiafulvalene (BEDT-TTF) and the Tris(Chloranilato)Ferrate(III) Complex. *Inorg. Chem.* **2014**, *53*, 7028–7039. https://doi.org/10.1021/ic501001r.

(33) Atzori, M.; Pop, F.; Auban-Senzier, P.; Clérac, R.; Canadell, E.; Mercuri, M. L.; Avarvari, N. Complete Series of Chiral Paramagnetic Molecular Conductors Based on Tetramethyl-Bis(Ethylenedithio)-Tetrathiafulvalene (TM-BEDT-TTF) and Chloranilate-Bridged Heterobimetallic Honeycomb Layers. *Inorg. Chem.* **2015**, *54*, 3643–3653. https://doi.org/10.1021/acs.inorgchem.5b00261.

(34) Ashoka Sahadevan, S.; Monni, N.; Abhervé, A.; Auban-Senzier, P.; Canadell, E.; Mercuri, M. L.; Avarvari, N. Synthesis and Physical Properties of Purely Organic BEDT-TTF-

Based Conductors Containing Hetero-/Homosubstituted Cl/CN-Anilate Derivatives. *Inorg. Chem.* **2017**, *56*, 12564–12571. https://doi.org/10.1021/acs.inorgchem.7b01994.

(35) Mercuri, M. L.; Congiu, F.; Concas, G.; Ashoka Sahadevan, S. Recent Advances on Anilato-Based Molecular Materials with Magnetic and/or Conducting Properties. *Magnetochemistry***2017**, *3*, 17, 1-56. https://doi.org/10.3390/magnetochemistry3020017.

(36) a) Sahadevan, S. A.; Abhervé, A.; Monni, N.; Sáenz de Pipaón, C.; Galán-Mascarós, J. R.; Waerenborgh, J. C.; Vieira, B. J. C.; Auban-Senzier, P.; Pillet, S.; Bendeif, E.-E.; Alemany, P.; Canadell, E.; Mercuri, M. L.; Avarvari, N. Conducting Anilate-Based Mixed-Valence Fe(II)Fe(III) Coordination Polymer: Small-Polaron Hopping Model for Oxalate-Type Fe(II)Fe(III) 2D Networks. *J. Am. Chem. Soc.***2018**, *140*, 12611–12621. https://doi.org/10.1021/jacs.8b08032. b) Sahadevan, S. A.; Monni, N.; Abherve,́ A.; Cosquer, G.; Oggianu, M.; Ennas, G.; Yamashita, M.; Avarvari, N.; Mercuri, M. L. *Inorg. Chem.* **2019**, *58*, 20, 13988-13998 https://doi.org/10.1021/acs.inorgchem.9b01968

(37) Abrahams, B. F.; Hudson, T. A.; McCormick, L. J.; Robson, R. Coordination Polymers of 2,5-Dihydroxybenzoquinone and Chloranilic Acid with the (10,3)-A Topology. *Cryst. Growth Des.***2011**, *11*, 2717–2720. https://doi.org/10.1021/cg2005908.

(38) Murase, R.; Abrahams, B. F.; D'Alessandro, D. M.; Davies, C. G.; Hudson, T. A.; Jameson, G. N. L.; Moubaraki, B.; Murray, K. S.; Robson, R.; Sutton, A. L. Mixed Valency in a 3D Semiconducting Iron–Fluoranilate Coordination Polymer. *Inorg. Chem.***2017**, *56*, 9025–9035. https://doi.org/10.1021/acs.inorgchem.7b01038.

(39) Kitagawa, S. Coordination Compounds of 1,4-Dihydroxybenzoquinone and Its

Homologues. Structures and Properties. *Coord. Chem. Rev.***2002**, *224*, 11–34. https://doi.org/10.1016/S0010-8545(01)00369-1.

(40) Kingsbury, C. J.; Abrahams, B. F.; Auckett, J. E.; Chevreau, H.; Dharma, A. D.; Duyker, S.; He, Q.; Hua, C.; Hudson, T. A.; Murray, K. S.; Phonsri, W.; Peterson, V. K.; Robson, R.; White, K. F. Square Grid Metal – Chloranilate Networks as Robust Host Systems for Guest Sorption. *Chem. Eur. J.* **2019**, *25*, 5222–5234. https://doi.org/10.1002/chem.201805600.

(41) Brendan F. Abrahams; Grannas, M. J.; Hudson, T. A.; Hughes, S. A.; Pranoto, N. H.; Richard Robson. Synthesis, Structure and Host-Guest Properties of $(Et_4N)_2[Sn^{IV}$ Ca^{II} $(Chloranilate)_4]$, a New Type of Robust Microporous Coordination Polymer with a 2D Square Grid Structure. *Dalt. Trans.***2011**, *40*, 12242–12247. https://doi.org/10.1039/c1dt10876j.

(42) Benmansour, S.; Pérez-Herráez, I.; López-Martínez, G.; Gómez García, C. J. Solvent-Modulated Structures in Anilato-Based 2D Coordination Polymers. *Polyhedron***2017**, *135*, 17–25. https://doi.org/10.1016/j.poly.2017.06.052.

(43) Gómez-Claramunt, P.; Benmansour, S.; Hernández-Paredes, A.; Cerezo-Navarrete, C.; Rodríguez-Fernández, C.; Canet-Ferrer, J.; Cantarero, A.; Gómez-García, C. J. Tuning the Structure and Properties of Lanthanoid Coordination Polymers with an Asymmetric Anilato Ligand. *Magnetochemistry* **2018**, *4*, 6, 1-21. https://doi.org/10.3390/magnetochemistry4010006.

(44) Benmansour, S.; Hernández-Paredes, A.; Gómez-García, C. J. Effect of the Lanthanoid-

Size on the Structure of a Series of Lanthanoid-Anilato 2-D Lattices. *J. Coord. Chem.***2018**, *71*, 845–863. https://doi.org/10.1080/00958972.2017.1420182.

(45) Abrahams, B. F.; Coleiro, J.; Hoskins, B. F.; Robson, R. Gas Hydrate-like Pentagonal Dodecahedral $M_2(H_2O)_{18}$ Cages (M = Lanthanide or Y) in 2,5-Dihydroxybenzoquinone-Derived Coordination Polymers. *Chem. Commun.***1996**, *2*, 603-604. https://doi.org/10.1039/cc9960000603.

(46) Abrahams, B. F.; Coleiro, J.; Ha, K.; Hoskins, B. F.; Orchard, S. D.; Robson, R. Dihydroxybenzoquinone and Chloranilic Acid Derivatives of Rare Earth Metals. *J. Chem. Soc. Dalt. Trans.***2002**, *2*, 1586-1594. https://doi.org/10.1039/b109296k.

(47) Ashoka Sahadevan, S.; Monni, N.; Abhervé, A.; Marongiu, D.; Sarritzu, V.; Sestu, N.; Saba, M.; Mura, A.; Bongiovanni, G.; Cannas, C.; Quochi, F.; Avarvari, N.; Mercuri, M. L. Nanosheets of Two-Dimensional Neutral Coordination Polymers Based on Near-Infrared-Emitting Lanthanides and a Chlorocyananilate Ligand. *Chem. Mater.***2018**, *30*, 6575–6586. https://doi.org/10.1021/acs.chemmater.8b03399.

(48) Xu, J.; Chen, X.; Xu, Y.; Du, Y.; Yan, C. Ultrathin 2D Rare-Earth Nanomaterials: Compositions, Syntheses, and Applications. *Adv. Mater.* **2019**, *1806461*, 1–17. https://doi.org/10.1002/adma.201806461.

(49) Zhang, S.; Sunami, Y.; Hashimoto, H. Mini Review : Nanosheet Technology towards Biomedical Application. *Nanomaterials* **2017**, *7*, 1–7. https://doi.org/10.3390/nano7090246.

(50) Cui, Y.; Xu, H.; Yue, Y.; Guo, Z.; Yu, J.; Chen, Z.; Gao, J.; Yang, Y.; Qian, G.; Chen, B.

A Luminescent Mixed-Lanthanide Metal–Organic Framework Thermometer. *J. Am. Chem. Soc.***2012**, *134*, 3979–3982. https://doi.org/10.1021/ja2108036.

(51) Zhao, Y.; Wei, C.; Chen, X.; Liu, J.; Yu, Q.; Liu, Y.; Liu, J. Drug Delivery System Based on Near-Infrared Light-Responsive Release of Dexamethasone To Inhibit Inflammation and Treat Molybdenum Disulfide Nanosheets Controls the High-Efficiency Osteoarthritis. *ACS Appl. Mater. Interfaces***2019**, *11*, 11587–11601.

(52) Xiaoxiong, Z.; Wenjun, Z.; Cuiliu, L.; Xiaohong, Q.; Chengyu, Z. Eu^{3+} -Postdoped UIO-66-Type Metal–Organic Framework as a Luminescent Sensor for Hg^{2+} Detection in Aqueous Media. *Inorg. Chem.* **2019**, *58*, 3910–3915. https://doi.org/10.1021/acs.inorgchem.8b03555.

(53) Xu, H.; Gao, J.; Qian, X.; Wang, J.; He, H.; Cui, Y.; Yang, Y.; Wang, Z.; Qian, G. Metal-Organic Framework Nanosheets for Fast-Response and Highly Sensitive Luminescent Sensing of Fe^{3+}. *J. Mater. Chem. A* **2016**, *4*, 10900–10905. https://doi.org/10.1039/c6ta03065c.

(54) Abhervé, A.; Mañas-Valero, S.; Clemente-León, M.; Coronado, E. Graphene Related Magnetic Materials: Micromechanical Exfoliation of 2D Layered Magnets Based on Bimetallic Anilate Complexes with Inserted $[Fe^{III}(Acac_2\text{-Trien})]^+$ and $[Fe^{III}(Sal_2\text{-Trien})]^+$ Molecules. *Chem. Sci.* **2015**, *6*, 4665–4673. https://doi.org/10.1039/C5SC00957J.

(55) Benmansour, S.; Abhervé, A.; Gómez-Claramunt, P.; Vallés-García, C.; Gómez-García, C. J. Nanosheets of Two-Dimensional Magnetic and Conducting Fe(II)/Fe(III) Mixed-Valence Metal-Organic Frameworks. *ACS Appl. Mater. Interfaces* **2017**, *9*, 26210–26218.

https://doi.org/10.1021/acsami.7b08322.

(56) Bernal, M.; Álvarez, L.; Giovanelli, E.; Arnáiz, A.; Ruiz-González, L.; Casado, S.; Granados, D.; Pizarro, A. M.;Castellano-Gomez, A.; Pérez, E. M.Luminescent Transition Metal Dichalcogenide Nanosheets through One-Step Liquid Phase Exfoliation. *2D Mater.***2016**, *3*, 035014-1 – 11. doi:10.1088/2053-1583/3/3/035014

(57) Zhao, M.; Wang, Y.; Ma, Q.; Huang, Y.; Zhang, X.; Ping, J.; Zhang, Z.; Lu, Q.; Yu, Y.; Xu, H.; Zhao, Y.; Zhang, H. Ultrathin 2D Metal-Organic Framework Nanosheets. *Adv. Mater.***2015**, *27*, 7372–7378. https://doi.org/10.1002/adma.201503648.

(58) Lebedev, O. I.; Millange, F.; Serre, C.; Van Tendeloo, G.; Férey, G. First Direct Imaging of Giant Pores of the Metal-Organic Framework MIL-101. *Chem. Mater.***2005**, *17,* 6525–6527. https://doi.org/10.1021/cm051870o.

(59) Bünzli, J.-C. G. On the Design of Highly Luminescent Lanthanide Complexes. *Coord. Chem. Rev.***2015**, *293–294*, 19–47. https://doi.org/10.1016/j.ccr.2014.10.013.

(60) Quochi, F.; Saba, M.; Artizzu, F.; Mercuri, M. L.; Deplano, P.; Mura, A.; Bongiovanni, G. Ultrafast Dynamics of Intersystem Crossing and Resonance Energy Transfer in Er(III)−Quinolinolate Complexes. *J. Phys. Chem. Lett.* **2010**, *1*, 2733–2737. https://doi.org/10.1021/jz101044d.

(61) Quochi, F.; Orrù, R.; Cordella, F.; Mura, A.; Bongiovanni, G.; Artizzu, F.; Deplano, P.; Mercuri, M. L.; Pilia, L.; Serpe, A. Near Infrared Light Emission Quenching in Organolanthanide Complexes. *J. Appl. Phys.* **2006**, *99*, 053520-1–4. https://doi.org/10.1063/1.2177431.

(62) Tan, R. H.; Motevalli, M.; Abrahams, I.; Wyatt, P. B.; Gillin, W. P. Quenching of IR Luminescence of Erbium, Neodymium, and Ytterbium β-Diketonate Complexes by Ligand C−H and C−D Bonds. *J. Phys. Chem. B* **2006**, *110*, 24476–24479. https://doi.org/10.1021/jp0654462.

(63) Monguzzi, A.; Milani, A.; Mech, A.; Brambilla, L.; Tubino, R.; Castellano, C.; Demartin, F.; Meinardi, F.; Castiglioni, C. Predictive Modeling of the Vibrational Quenching in Emitting Lanthanides Complexes. *Synth. Met.* **2012**, *161*, 2693–2699. https://doi.org/10.1016/j.synthmet.2011.10.002.

(64) Artizzu, F.; Quochi, F.; Saba, M.; Loche, D.; Mercuri, M. L.; Serpe, A.; Mura, A.; Bongiovanni, G.; Deplano, P. Silica Sol–Gel Glasses Incorporating Dual-Luminescent Yb Quinolinolato Complex: Processing, Emission and Photosensitising Properties of the 'Antenna' Ligand. *Dalt. Trans.* **2012**, *41*, 13147-13153. https://doi.org/10.1039/c2dt30323j.

(65) Maka, V. K.; Mukhopadhyay, A.; Savitha, G.; Moorthy, J. N. Fluorescent 2D Metal-Organic Framework Nanosheets (MONs): Design, Synthesis and Sensing of Explosive Nitroaromatic Compounds (NACs). *Nanoscale* **2018**, *10*, 22389–22399. https://doi.org/10.1039/c8nr04992k.

(66) Zhang, S.; Du, D.; Qin, J.; Bao, S.; Li, S. A Fluorescent Sensor for Highly Selective Detection of Nitroaromatic Explosives Based on a 2D , Extremely Stable , Metal – Organic Framework. *Chem. Eur. J.* **2014**, *20*, 3589–3594. https://doi.org/10.1002/chem.201304692.

(67) Lian, X.; Zhao, D.; Cui, Y.; Yang, Y.; Qian, G. A near Infrared Luminescent Metal-Organic Framework for Temperature Sensing in the Physiological Range. *Chem. Commun.* **2015**, *51*, 17676–17679. https://doi.org/10.1039/c5cc07532g.

(68) Horcas, I.; Fernández, R.; Gómez-Rodríguez, J. M.; Colchero, J.; Gómez-Herrero, J.; Baro, A. M. WSXM: A Software for Scanning Probe Microscopy and a Tool for Nanotechnology. *Rev. Sci. Instrum.* **2007**, *78*, 013705-1–12. https://doi.org/10.1063/1.2432410.

SYNOPSIS

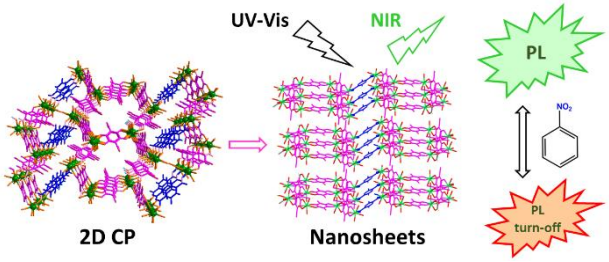

TOC

Supporting Information.

Figure S1 shows the coordination geometry of the two crystallographically independent Yb1 and Yb2 centers in compound **1** and a view of hexagonal and rectangular cavities; the H contacts of Yb^{III}•••C-H oscillators present in the unit cell, within 4-5 Å, which are responsible of Yb^{III} emission quenching, are also shown. In **Table S1**, Yb^{III}•••C-H distances below 5 Å are reported for compound **1**. In **Figure S2** the void space along the *b* axis, present in the structure of **1** (porous CP), is shown. **Figure S3** shows the dodecahedron geometry of Yb^{III} center in **2** along with a view of one layer; the H contacts of Yb^{III}•••C-H oscillators within 3-5 Å, present in the unit cell, are also shown. In **Table S2,** Yb^{III}•••C-H distances below 5 Å are reported for compound **2**. In **Section S1** the thickness of a monolayer (ho) and interlayer distances (d) for **1−2** compounds are calculated from crystal structures. In **Figure S4** and **Figure S5** reticular planes (3 0 0), observed at 2.98 Å and (1 -3 3), observed at 2.98 Å, are reported for compound **1** and **2** respectively. In **Figure S6** PXRD patterns of nanosheets and bulk for compounds **1** and **2** are reported along with their theoretical patterns calculated by CIF data. In the **EXPERIMENTAL SECTION** the Syntheses of bulk CP **1** and **2** and their single-crystal X-Ray Crystallography; the Syntheses of Nanosheets (1-2-NS) along with their Morphological, Optical and Photophysical Characterization are reported.